Modeling of Damage in Coilable Composite Shell Structures

Armanj D. Hasanyan* and Sergio Pellegrino†

California Institute of Technology, Pasadena, CA, 91125, USA

Coilable composite shell structures, composed of ultra-thin laminates, are ideal for deployable space structures applications. Their ability to be flattened and coiled for packaging, and deployed in their operational configuration makes them suitable for many space missions. Due to the complex states of stresses that occur in a composite shell during these processes (coiling, stowage, and deployment), material failure may be induced. This in turn would negatively affect the deployment, cause shape distortions, reduce the stiffness of the shell, or even lead to catastrophic failure of the mission. Therefore, predicting the failure modes and mechanisms of ultra-thin laminates at the structural scale is critical for design and certification purposes. However, this is often complicated by the complex microstructure and the multiple length-scales (micro and meso) associated with composites. This study presents a finite element model with progressive damage that effectively captures the ply failure modes. This is done through a damage constitutive model, where local cracks in the shell are smeared within a finite element. The fracture properties of interest are experimentally measured and incorporated into the model. The salient features of the model needed to capture failure are identified by comparing the simulation results with experiments. This is achieved by analysing the coiling of a TRAC longeron shell structure.

I. Introduction

Coilable thin shells made of composite materials are increasingly being used as a lightweight and cost-effective means of making large, deployable space structures. Examples include the Collapsible Tube Mast (CTM) booms in solar sails [1], the Storable Tubular Extendible Members (STEM) booms in the Roll Out Solar Array (ROSA) [2], the Triangular Rollable And Collapsible (TRAC) longerons in the Space Solar Power Project (SSPP) [3], [4], and other space-based reflectors and antennas [5], [6]. Unlike traditional composites, those used in these space applications are made of ultra-thin, high strain composites (HSC) plies. The laminates in the shells are usually made of 2 to 8 plies, which provide sufficient stiffness to the structure in the deployed configuration, while being able to be flattened and coiled for packaging.

Despite the thinness of these laminates, the design of the overall space structure and its packaging efficiency is often constrained by material failure in the HSC under large curvature loads. For example, failure can be induced by large localized stresses that appear due to local buckling in the shell during coiling [7], [8] or curvature concentrations near cutouts during folding [9]. At the structural scale, failure in the HSC appears as localized cracks. For example, the formation and propagation of such cracks was discussed in [10], where a Flattening to Rupture (FTR) test was introduced to observe the crack formation and propagation in HSC samples both at the macro and micro scales. During the crack formation and propagation, multiple failure modes, across multiple length scales were seen. These include kinking, fiber breakage, fiber-matrix debonding, localized delamination, etc.

In this study, a continuum-based progressive damage model is proposed for deployable shell structures to predict the formation and propagation of the cracks. In the past, damage models have been developed to predict the onset of failure and post-failure response of fiber-reinforced materials. The approach has mostly been used to model the composite at the meso-scale (ply scale) for material design and certification [11], [12]. However, due to the discrete nature of cracks in HSC (crack width 100 μm to 300 μm), the damage is assumed to be smeared within a shell element of the numerical model. The crack formation and propagation are represented using a softening constitutive response, based on the material strength and fracture toughness properties. This approach provides a numerically efficient approach for predicting material failure in deployable shell structures made of HSC at the structure scale, for design purposes.

---

*Assistant Professor, Department of Aerospace and Mechanical Engineering, The University of Texas at El Paso, 500 W. University Ave, El Paso, TX 79968. AIAA Member.

†Joyce and Kent Kresa Professor of Aerospace and Civil Engineering, Graduate Aerospace Laboratories, 1200 E California Blvd. MC 105-50, Pasadena. AIAA Fellow.

The structure of interest is the TRAC longeron shown in Fig. 1 a. This structure is currently being considered for various space missions. To simplify the analysis, the problem considered is the coiling of a single longeron structure around a rigid cylindrical hub of radius R. During the coiling process, a constant tension load T is applied to ensure the structure conforms to the hub. The details of the boundary value problem will be elaborated in the following sections.

The cross-section of the TRAC longeron is shown in Fig. 1 b. It consists of two curved flanges (outer and inner flange), bonded together at the web-region. The geometric parameters characterizing the cross-section include the flange radius r, flange opening angle θ, and web width w. In this study, the flanges of the longeron consist of 3-plies, with [0/90/0] orientation, where the 0° is along the length of the longeron (x-axis). The flanges meet at the web region, which is composed of 7-plies.
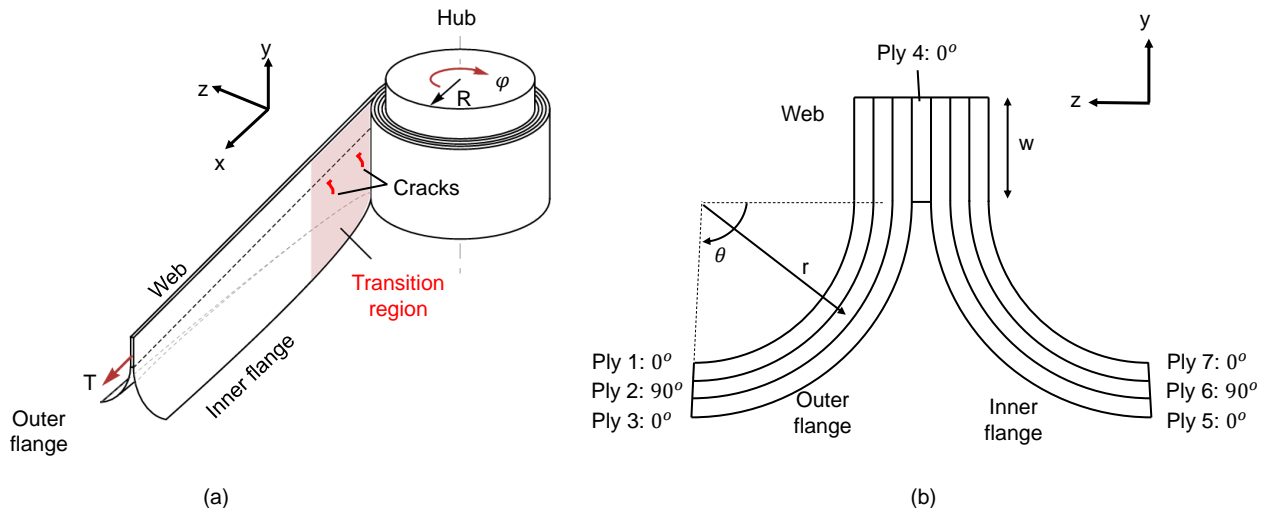
Fig. 1   Schematic of the longeron structure, showing (a) the details of the coiling setup [13], and (b) the cross-section and the plies of the flange and the web regions.

To increase the packaging efficiency of the structure, minimizing the hub radius is desired. However, as the hub is rotated by the angle φ during the coiling process, localized curvatures (and stresses) are observed in the transition region. The location of the transition region is shown in Fig. 1 a, where the cross-section goes from an unflattened state to a flat state. In the transition region, a localized buckle is observed at the inner flange of the longeron. The mechanics for the buckle formation and propagation have been thoroughly analyzed experimentally and numerically in [7], [13]. The resulting material failure associated with the stress concentrations in the transition region is discussed in [7], [8]. These include the formation of localized surface cracks at the inner flange of the longeron.

To predict the formation and propagation of these cracks during the coiling process, a progressive damage model is considered. Then, to verify the structure-scale numerical prediction, a coiling experiment is also conducted on the longeron. The coiling experiments and the resulting material failure are discussed in Section II. In Section III, the details of the damage constitutive model for the shell are outlined. In addition, the experimentally measured linear elastic, strength, and fracture properties for defining the constitutive model are given. In Section IV, the finite element simulation of the longeron structure is shown along with the predicted failure modes. The salient features of the numerical model are outlined, along with verification of the results with experiments. In Section V, conclusions of the results along with approaches to improve the model in future work are discussed.
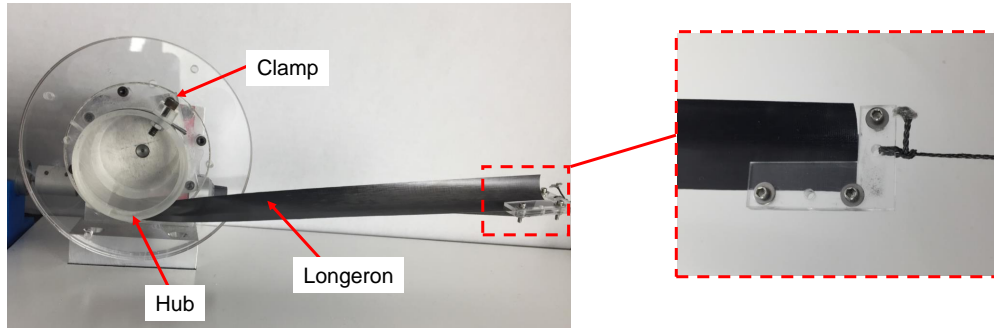
II. Coiling Experiment

A. Test Setup
To validate the simulation results in the following Section. IV, coiling experiments were first conducted on TRAC longerons. For the experiments, four longerons of 400 mm length were manufactured and tested. The post-cure cross-sectional dimensions were $r = 10.6$ mm, $\theta = 105^o$, and $w = 8$ mm. The laminate layup in the flange and web

regions is shown in Fig. 1 b. The unidirectional plies of the longeron comprised of T800 carbon fibers, with NTPT ThinPreg 402 epoxy resin. The autoclave manufacturing steps and processes considered to make the structures are detailed in [14].

The experimental setup for coiling is shown in Fig. 2. In the setup, the longeron structure was coiled around a rigid (acrylic) hub of radius $R = 25.4$ mm. The hub radius was selected based on the minimum radius at which material failure was visually observed after coiling. Prior to coiling, the left-end of the longeron was attached to the hub by clamping it between the hub and an acrylic clamp. A uniform tension load of T = 15 N was applied at the right end of the longeron through a hanging weight and pulley system to ensure it conformed to the hub during the coil process. The hub was also attached to an electric motor, through which quasi-static coiling was imposed at a rate of 0.5 RPM. Further details regarding the experimental setup are outlined in [7], [14], [15].

Fig. 2   Experimental setup for coiling the longeron structure. Uniform tension is applied throughout coiling at the right-end side using a hanging weight pulley system (not in view).

To prevent the inner flange from making contact with the clamp, the longeron was limited to less than a single revolution of coiling. During this process, a localized buckle was observed at the transition region of the inner flange. The buckle was first observed after rotating the hub for $\varphi = 100^o$. The buckle grew in amplitude and propagated throughout the inner flange up to the coiling limit of $\varphi = 270^o$.

B. Experimental Results

After coiling and uncoiling the longerons using the test setup, visible cracks were observed at the inner flange region. As shown in Fig. 3 a, the visible cracks were located near the web-flange intersection. The cracks are attributed to a local stress concentration that develops in this region due to the local buckling of the inner flange. The formation and propagation of the local buckle will be shown in the numerical simulation of coiling in Section IV. The visible cracks were measured to be between 2 mm to 4 mm in length. Similar observations of localized cracks were made in all four longerons after coiling.

In addition to the visible surface cracks, micro-cracks were also detected inside the longerons after coiling. To observe these, the microstructure of the four longerons were imaged using a ZEISS Xradia VersaXRM-510 CT scanner. The area of interest was 4 mm × 4 mm × 44 mm along the web-flange intersection region. To detect damage, all four longerons were scanned both before and after coiling at the same location. By comparing the 3D volume images of the scanned regions, small micro-cracks of approximately 0.192 mm in size were detected throughout the coiled length. A representative comparison of the microstructure of the longeron near the web-flange intersection region before and after coiling is shown in Fig. 3 a and b, respectively. Because these micro-cracks are small in size and are located inside the longeron thickness, they were not visible with the naked eye. Despite this, the development of micro-cracks due to coiling can serve as local stress concentration for further crack growth during the operation of the structure.

III. Constitutive Model for Damage and Material Properties

In this section, the details of the model for predicting material failure in the composite shell structure are discussed. Material failure is modeled through damage variables in the constitutive relation of each ply. The formation and propagation of the cracks is represented by a bilinear constitutive relation, where the softening region is controlled by damage variables. In this approach, the cracks in the shell are assumed to be smeared over a numerical finite element.
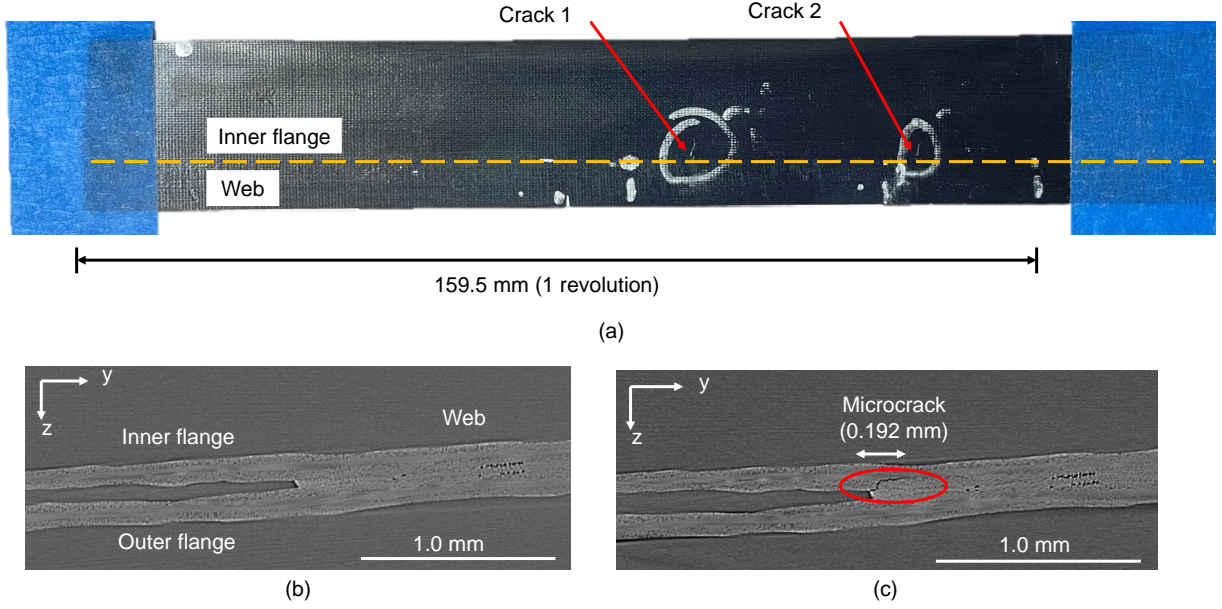
Fig. 3 Damage in the longeron after coiling. Visible surface cracks 2 - 4 mm long observed at the inner flange, near the web (a). Micro-CT images of the longeron cross-section (b) before coiling and (c) after coiling, with the formation of a micro-crack.

This approach provides a numerically efficient modeling framework for predicting material failure in the composite shell longeron structure during coiling.

A. Constitutive Model for Damage

The theoretical background for defining a constitutive model for fiber reinforced composites that accounts for damage is outlined in [16]. For each ply of a general N-layered laminate, the orthotropic compliance relation under plane stress has the form

$$\{\varepsilon\} = [S(d)]\{\sigma\} \tag{1}$$

where $\{\varepsilon\} = \{\varepsilon_{11}\ \varepsilon_{22}\ 2\varepsilon_{12}\}^T$ and $\{\sigma\} = \{\sigma_{11}\ \sigma_{22}\ \sigma_{12}\}^T$ are the strain and stress components, respectively. The compliance matrix $[S(d)]$ is defined as

$$[S(d)] = \begin{bmatrix} \frac{1}{(1-d_{11})E_{11}} & -\frac{v_{21}}{E_{11}} & 0 \\ -\frac{v_{12}}{E_{22}} & \frac{1}{(1-d_{22})E_{22}} & 0 \\ 0 & 0 & \frac{1}{(1-d_{12})G_{12}} \end{bmatrix} \tag{2}$$

Here, E_{11} and E_{22} are the linear elastic moduli along the longitudinal (fiber) and transverse directions, respectively, and G_{12} is the in-plane shear modulus. The Poisson's ratios are v_{12} and v_{21}. In the compliance matrix, the damage is taken into account through the parameters d_{11}, d_{22}, and d_{12}. In this study, the damage variables correspond to the different failure modes of a ply, which are fiber tension (mode I), fiber compression (mode II), matrix tension and shearing (mode III), and matrix compression and shearing (mode IV). The damage modes of the ply are detected through Hashin's criterion [17], which are expressed as:

Mode I, fiber tension

$$F_f^T = \left(\frac{\sigma_{11}}{X^T}\right)^2, \quad \sigma_{11} > 0 \tag{3}$$

Mode II, fiber compression

$$F_f^C = \left(\frac{\sigma_{11}}{X^C}\right)^2, \quad \sigma_{11} < 0 \tag{4}$$

4

Mode III, matrix tension and shearing

$$F_m^T = \left(\frac{\sigma_{22}}{Y^T}\right)^2 + \left(\frac{\sigma_{12}}{S}\right)^2, \quad \sigma_{22} > 0 \tag{5}$$

Mode IV, matrix compression and shearing

$$F_m^C = \left(\frac{\sigma_{22}}{Y^C}\right)^2 + \left(\frac{\sigma_{12}}{S}\right)^2, \quad \sigma_{22} < 0 \tag{6}$$

$F_f^T, F_f^C, F_m^T, F_m^C$ are failure indices for each respective mode, which assume a value of 1 when failure initiates, and $X^T, X^C, Y^T, Y^C, S = 0.5Y^C$ are the fiber tension, fiber compression, matrix tension, matrix compression, and in-plane shear strengths of the ply, respectively. Here σ_{11} is the stress along the fiber direction, σ_{22} is transverse to the fibers, and σ_{12} is the in-plane shear. It should be noted that in mode III and mode IV, the matrix tension and compression stresses, respectively, and in-plane shear stress are assumed to be mutually weakening.

In Eqn. 2, d_{11}, d_{22}, and d_{12} represent the damage variables corresponding to fiber, matrix, and in-plane shear modes, respectively. To differentiate the tension and compression failure modes along the longitudinal and transverse directions, they are further expressed as

$$d_{11} = \begin{cases} d_f^T & \text{if } \sigma_{11} > 0 \\ d_f^C & \text{if } \sigma_{11} < 0 \end{cases} \tag{7a}$$

$$d_{22} = \begin{cases} d_m^T & \text{if } \sigma_{22} > 0 \\ d_m^C & \text{if } \sigma_{22} < 0 \end{cases} \tag{7b}$$

$$d_{12} = 1 - (1 - d_f^T)(1 - d_f^C)(1 - d_m^T)(1 - d_m^C) \tag{7c}$$

where d_f^T, d_f^C, d_m^T, and d_m^C are the fiber tension, fiber compression, matrix tension, and matrix compression failure modes, respectively. In addition, the in-plane shear is expressed in terms of these damage variables.

For each failure mode, the evolution of damage is based on an energy-based bilinear constitutive relation between equivalent stresses and strains. The schematic of it is shown in Fig. 4. Prior to the peak load, the relation between the stresses and strains are linear elastic. In this region of loading, the damage variable assumes a value of 0. Once the peak load is reached, or Hashin's criterion is satisfied for a specific mode, the corresponding damage variable monotonically increases towards a maximum value of 1. When a value of 1 is reached, the stiffness for that mode at a given material point is effectively zero.
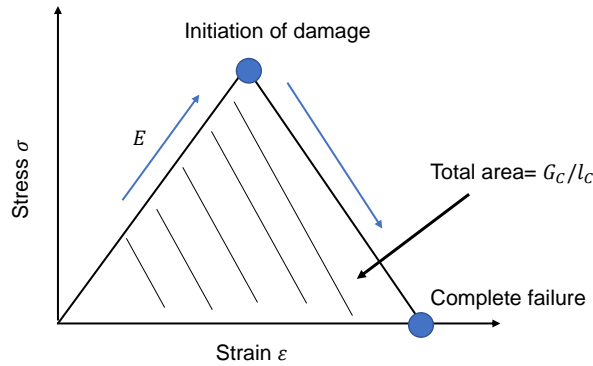
Fig. 4 Schematic of bilinear constitutive relation between effective stress and strain for each ply failure mode.

The softening relation in the bilinear constitutive model for a given mode is based on the fracture energy dissipated during the damage process, i.e. G_C. Therefore, in the finite element analysis, the area under the bilinear relation is assumed to correspond to G_C/l_C, where l_C is the characteristic length of a shell element. The length scale l_C is introduced to alleviate mesh dependency during material softening, according to the crack band model by Bažant and Oh

[18]. In the following numerical analysis, l_C is considered to be the square root of the finite element area at an integration point. By including the characteristic element length into the constitutive relation, a constant dissipated fracture energy is achieved, regardless of the element dimensions. Further details regarding the damage model considered in this study are outlined in [11], [16], and [19].

B. Linear Elastic, Strength, and Fracture Toughness Properties

To define the bilinear constitutive relation for each failure mode, experiments were conducted to estimate the linear elastic, strength, and fracture toughness properties of the ply. The experiments were done on laminate systems composed of the same plies as those used to make the TRAC longeron structures (T800 carbon fibers embedded in NTPT ThinPreg 402 epoxy resin). The test samples for material characterization were manufactured by layering prepregs on a flat rectangular plate and curing in an autoclave. To infer the linear elastic properties of a single ply, tests were done on a 7-ply unidirectional laminate system ($[0_7]$) in accordance to ASTM D3039. The summary of the linear elastic properties of the $[0_7]$ laminate are given in Table 1. The linear elastic properties of the ply were also reported in [20].

Table 1   Linear elastic properties of a $[0_7]$ laminate system, or an equivalent ply layer.

E_{11} [MPa]	E_{22} [MPa]	G_{12} [MPa]	ν_{12}
128,000	6,500	7,500	0.35

Next, experiments were also conducted to determine the strength properties of the ply. The ply strength properties of interest include longitudinal (fiber) tension X^T, longitudinal (fiber) compression X^C, transverse (matrix) tension Y^T, and transverse (matrix) compression Y^C. When defining these properties, it should be noted that when the ply is under in-plane tension and compression loading conditions along these directions, the failure stress of the ply is much lower when compared to the failure stress when embedded in a laminate or under large curvature loads. This phenomenon is attributed to size effects that occurs at the meso-scale. Therefore, the ply strengths cannot be treated as intrinsic ply properties, but as in situ properties that depend on the laminate orientation, geometry, and loading conditions (in-plane loading vs bending) [21], [22].

As a result, a more accurate estimation of the ply strength values was obtained by conducting large curvature experiments on a $[0_7]$ laminate system. The tests were done using the column bending test (CBT) fixtures. Details regarding the experimental setup and approaches are outlined in [23] and [24]. In the test setup, the CBT fixtures were used to induce an almost-uniform curvature on the rectangular test samples. The $[0_7]$ test laminates were tested along the longitudinal and transverse directions. Because the failure of the laminate system was found to be induced by the failure of the surface plies, the critical surface stresses were estimated using the following formulas from classical lamination theory

$$\sigma_{11,cr}^{surf} = \frac{E_{11}t}{2(1 - v_{12}v_{21})}\kappa_{11,cr} \tag{8a}$$

$$\sigma_{22,cr}^{surf} = \frac{E_{22}t}{2(1 - v_{12}v_{21})}\kappa_{22,cr} \tag{8b}$$

where $\kappa_{11,cr}$ and $\kappa_{22,cr}$ are the critical curvature values along the principal directions that were measured from the CBT experiments, $t = 210 \ \mu$m is the total nominal thickness of the 7-ply laminate, and $\sigma_{11,cr}^{surf}$ and $\sigma_{22,cr}^{surf}$ are the surface stresses along the longitudinal and transverse directions, respectively. From the surface stresses, the ply strength values under large curvature loads were estimated to be $\sigma_{11,cr}^{surf} = X^T = X^C$ and $\sigma_{22,cr}^{surf} = Y^T = Y^C$. Under the following assumption, the tension and compression strength of the ply are assumed to be equal. Despite this, the following assumption provides the best estimate of the (in situ) ply strength under large curvature loads. The strength values along the longitudinal and transverse directions are summarized in Table 2.

Table 2   Estimation of in situ ply strength properties under large curvature loading conditions.

X^T [MPa]	X^C [MPa]	Y^T [MPa]	Y^C [MPa]
2840	2840	76	76

The estimations of the tension and compression fracture toughnesses of the ply along the longitudinal and transverse directions are reported in Table 3. Along the transverse direction, the tension (G_m^T) and compression (G_m^C) fracture toughness, respectively, are assumed to be equal to the mode I inter-laminar (interface) fracture toughness of the NTPT ThinPreg 402 epoxy resin, which was reported in [25]. In addition, along the fiber direction, the tension (G_f^T) and compression (G_f^C) fracture toughness are estimated from the bending mode fracture toughness tests. This was determined by conducting CBT experiments on samples with an initial notch. In the present study, the values of G_f^T and G_f^C are set equal for simplicity.

Table 3   Estimation of fracture toughness values of the ply in the large curvature regime.

G_f^T [kJ/m^2]	G_f^C [kJ/m^2]	G_m^T [kJ/m^2]	G_m^C [kJ/m^2]
30.1	30.1	0.315	0.315

In summary, by using the linear elastic, estimated (in situ) strength, and fracture toughness properties given in Table 1, Table 2, and Table 3, respectively, the bilinear constitutive relation of the ply can be defined for each failure mode. Next, the details of the finite element model for longeron coiling are discussed.

IV. Simulation Results and Damage Predictions

The finite element model of the longeron was made using the Abaqus 2020 software. The cross-sectional dimensions of the 400 mm longeron were considered to be the same as those measured in Section II (i.e. $r = 10.6$ mm, $\theta = 105^o$, and $w = 8$ mm). The structure was modeled using S4R shell elements. In addition, the cylindrical hub of radius $R = 25.4$ mm and height of 50 mm was modeled using 3D rigid elements (R3D4). The analysis was done using a dynamic implicit solver, with a general contact (frictionless) interaction. The finite element model of coiling considered is based on the model proposed in [7].

In modeling the structure, a single S4R shell element was used to represent the three plies of the outer and the inner flange regions (see Fig. 1 b). As a result, ply 1, ply 2, and ply 3 were modeled with a single S4R shell element in the thickness direction. Similarly, ply 5, ply 6, and ply 7 of the inner flange were modeled by a separate set of S4R shell elements. In the web region, the outer and inner flange elements were bonded (tie constraint) to the top and bottom surfaces of an additional set of S4R shell elements representing ply 4. In the analysis, shell elements with areal dimensions of 1 mm × 1 mm were considered. This element size was selected by conducting numerical convergence studies on the mesh size to achieve converged values for the local stresses in the transition region.

To replicate the coiling processes, the simulation was divided into three distinct steps, shown in Fig. 5. In step 1, the left end of the longeron was flattened by applying a uniform pressure load P on the top surface of the upper flange and moving the rigid hub upwards. In step 2, a uniform tension load of 15 N was applied at the right end of the longeron. While maintaining these loads, in step 3 the longeron is coiled around the hub. This was done by applying a quasi-static rotation at the center of the rigid hub.

In addition, the spatial variation of local imperfections in the shell was also incorporated into the model. This was done to introduce a mechanism for failure localization in the shell during coiling. From the micro-CT images taken prior to coiling (discussed in Section II), the composite shell thickness was seen to have a significant spatial variation. The thickness imperfection is attributed to the manufacturing process, where a resin flow in induced in the thickness direction to remove excess resin in a composite part. Because the spatial variation of thickness was assumed to have the most prominent effect on the localization of cracks in the shell (in comparison to volume fraction, fiber orientation, strength, etc.), it was introduced into the shell model. This was done by assigning a value of thickness at each integration point in the shell element based on a Gaussian random number generator.

The random number generator was based on the mean and standard deviation of the thicknesses measured from the micro-CT images. From 100 measurement taken from the flange and web regions, the thickness values are reported in Table 4. As seen, the web region of the longeron is fairly uniform, with a mean thickness value of 212 μm and a standard deviation of 11 μm (5.3 % of the mean). In comparison, the flange regions have a mean thickness value of 88 μm, with a significantly higher standard deviation of 14 μm (16.3 % of the mean). As a result, the spatial variation of the thickness was introduced only in the flange regions of the structure. A single rendition, or realization of the longeron structure with random thicknesses assigned based on the Gaussian Gaussian random number generator is shown in Fig. 6. In the following study, the results of four different renditions of the longeron are presented. The response of
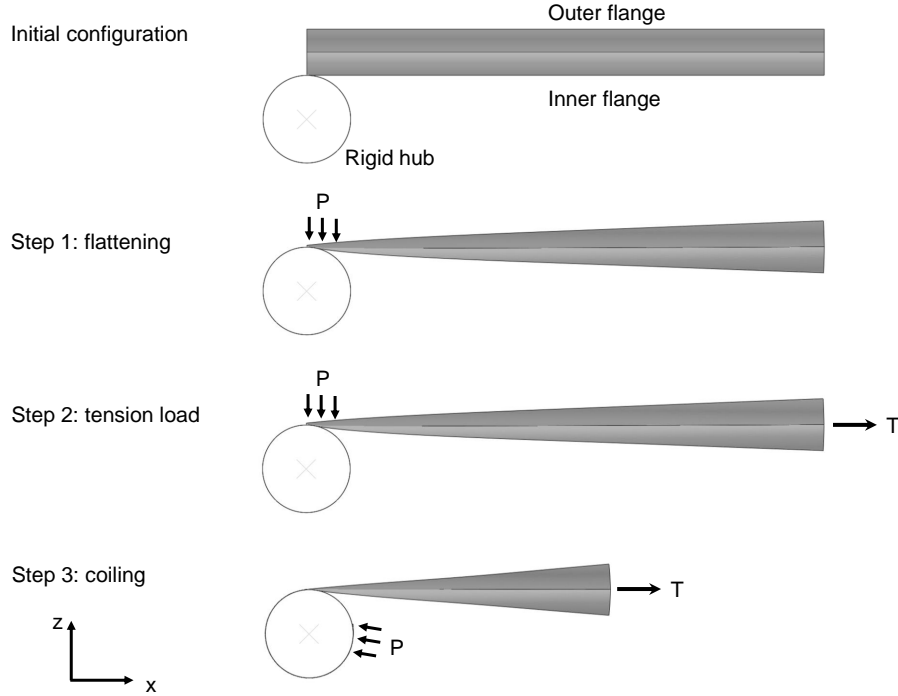
Fig. 5   Steps for numerically modeling the coiling process of the longeron shell structure.

the longeron with a uniform flange thickness and its comparison with the different renditions of the longerons will be discussed in the next section.

**Table 4   Laminate thickness measurements at the flange and web regions of the longeron.**

	Mean thickness (μm)	Standard deviation (μm)	Maximum thickness (μm)	Minimum thickness (μm)
Flange	88	14	125	41
Web	212	11	241	183

### A. Stress Analysis of the Transition Region

Before introducing the finite element predictions of damage, the following subsection will discuss the local stress concentration that develops in the longeron as a result of the formation and propagation of the localized buckle in the transition region. For this analysis, only the linear elastic properties of the plies (Table 1) will considered. In Fig. 7 a and b, the results for the longeron with uniform curvature are shown, at hub rotation values of $\varphi = 100^o$ and $\varphi = 360^o$, respectively. In Fig. 7 c and d, the results of the longeron with thickness imperfections (rendition 1) are shown at rotations values of $\varphi = 100^o$ and $\varphi = 360^o$, respectively. In these figures, because the localized buckle forms in the inner flange of the longeron, the outer flange has been removed. Contours in the figure show the change in the transverse curvature $\Delta\kappa_{22}$.

As seen in Fig. 7 a and c, the buckle is formed after applying a coiling angle $\varphi = 100^o$ in both longerons with uniform and nonuniform thickness cases. Upon further coiling the structure to $\varphi = 360^o$ (Fig. 7 b and d), the amplitude of the buckle is seen to increase monotonically. Comparing the results of the longeron with uniform and nonuniform flange thicknesses, it can be seen that the thickness imperfection did not have effect on the formation, propagation, and the shape of the overall localized buckle.

The difference between the results of the longeron with uniform and nonuniform flange thicknesses can be seen in the values of the local stresses at the transition region. In Fig. 8, the maximum values of the stresses in the transition
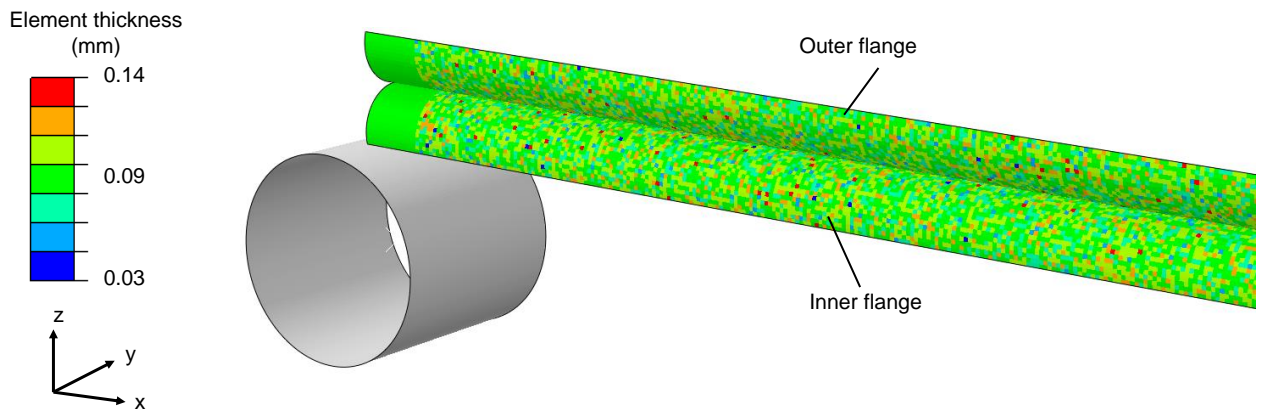
Fig. 6   Visualization of a single rendition of a longeron structure with spatial thickness distribution on an element basis.
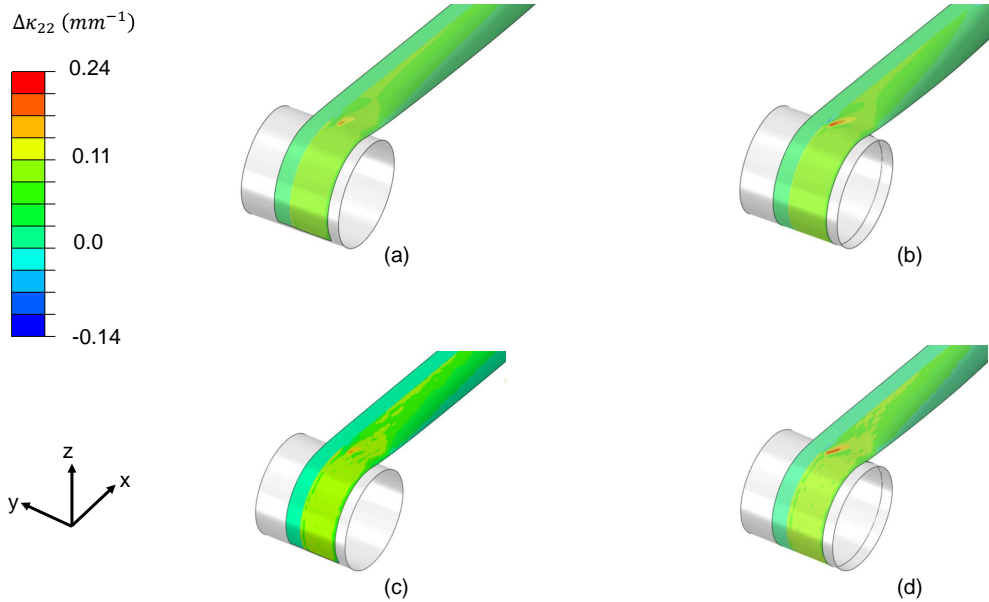
Fig. 7   Formation of the localized buckle at the transition region of the longeron with uniform thickness after coiling for (a) $\varphi = 100^o$ and its propagation after coiling for (b) $\varphi = 360^o$. Similarly, the buckle formation in the longeron with nonuniform thickness (rendition 1) after coiling for (c) $\varphi = 100^o$, and its propagation after coiling to (d) $\varphi = 360^o$.

region are plotted for a given coiled configuration, or hub rotation φ. The two relevant stresses that are shown include the transverse tension stress in ply 7 (Fig. 8 a) and the transverse compression stress in ply 5 (Fig. 8 b).

When looking at the stresses in the longeron with uniform thickness (shown in red), it can be seen that the values are below the critical ply strength ($Y^T = Y^C = 76$ MPa). As a result, no element failure was observed in the structure. However, in the longeron with thickness imperfection, it can be seen that the stresses in the transition region fluctuate as the longeron is coiled. These element-based fluctuations of the stresses often exceed the critical strength values. In Fig. 8 a and b, four different renditions of the longeron with nonuniform thicknesses is shown. As it will be shown in the following subsection, these local fluctuation of the stresses induce failure localization in the shell, which correspond to the material failure observed in the experiments (Section II).
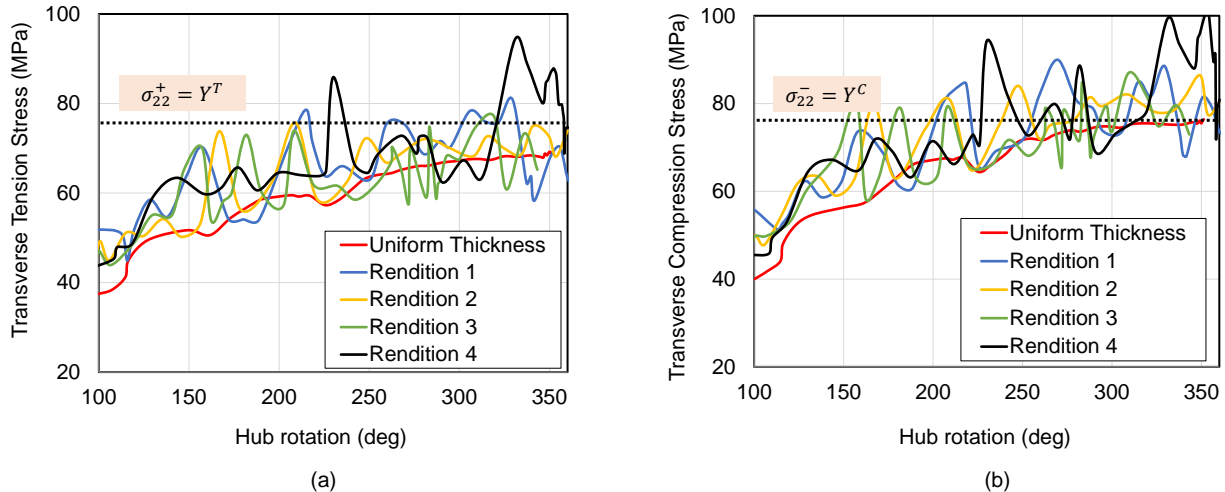
Fig. 8   The maximum transverse tension stress in ply 7 (a) and the maximum compression stress in ply 5 (b) in the transition region of the longeron for different coiled configurations.

B. Coiling Simulation Results With Damage

Next, the results of the coiling simulation with the damage constitutive model implemented are shown. The details of the bilinear constitutive model and the estimated properties based on experiments were discussed in Section III.

As shown in Fig. 8, the local stress values on an element basis exceed the critical strength of the ply. As a result, the simulations of the longeron structures were redone, but now with the bilinear constitutive relations. For the longeron structure with uniform thickness, no damage was detected, since the stress values in the structure were far below the critical. However, in the longerons with nonuniform thicknesses, material failure was detected. The results of the longerons for the four different renditions are shown in Fig. 9 and Fig. 10. Because material failure was found in the inner flange only, the outer flange has been removed for visualization. The failed elements, shown in red, are highlighted on the longeron in the uncoiled configuration. In the figures, only the coiled region of the structure (159.5 mm length or $\varphi = 360^o$) is shown.

In Fig. 9, the elements with failure in ply 7 is shown. The elements highlighted in red correspond to mode III, where the damage variable has reached a value of 1 ($d_{22} = d_m^T = 1$). Similarly, in Fig. 10, the red elements correspond to failure in ply 5. The elements in red in Fig. 10 correspond to mode IV failure, where the damage variable $d_{22} = d_m^C = 1$. No additional failure modes were detected in the longerons.

In comparing the simulation results in Fig. 9 and 10 to the experiments in Fig. 3, it can be seen that the failure is localized in the inner flange region, near the web-flange intersection region. The first failure is detected after coiling the longerons approximately by $\varphi = 180^o$. This is due to buckle formation at $\varphi = 100^o$ and its growth to a critical value at approximately $\varphi = 180^o$.

Some discrepancies between the model and the experiment should also be noted. Most noticeably, the predictions of failure in the model are more sparsely populated throughout the length of the longeron, whereas in the experiment, two
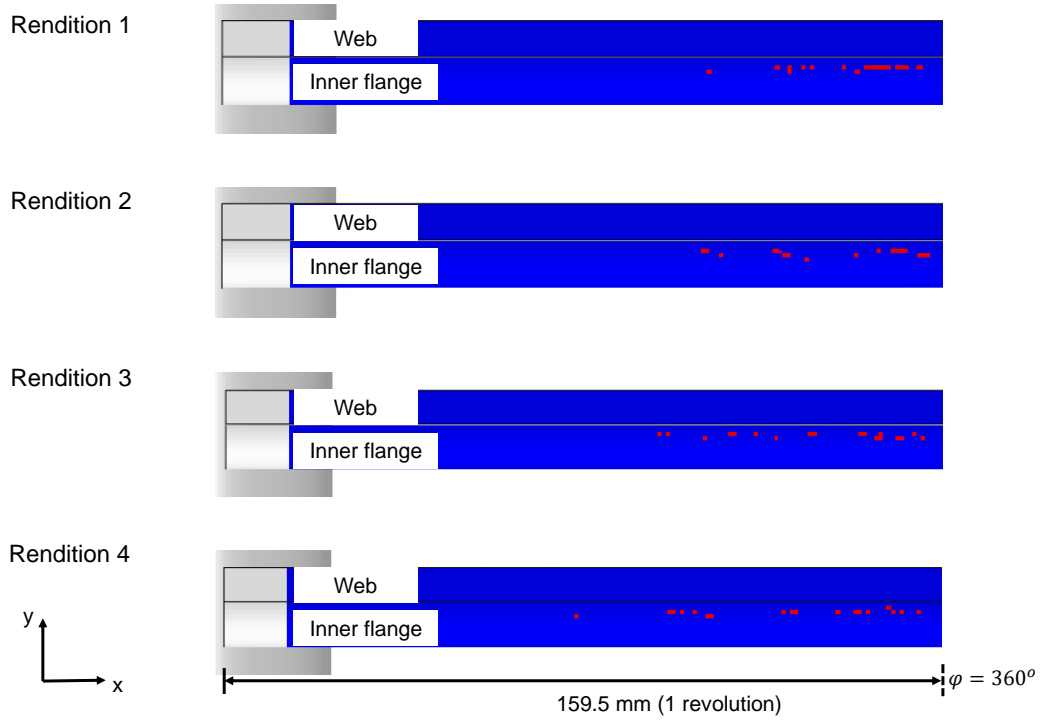
Fig. 9   Highlighted elements (shown in red) of the inner flange shell where failure has occurred in ply 7 due to matrix tension (mode III).
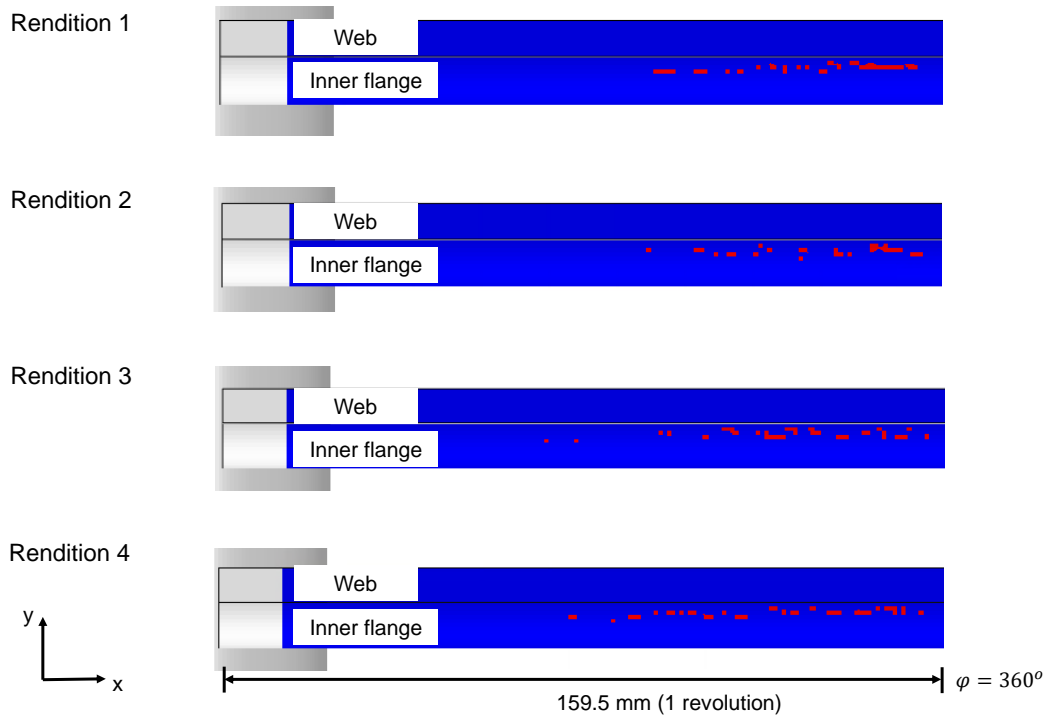
Fig. 10   Highlighted elements (shown in red) of the inner flange shell where failure has occurred in ply 5 due to matrix compression (mode IV).

cracks of length 2 mm to 4 mm were detected. However, the predictions of the finite element model are thought to not only represent the macro-cracks observed visually in the structure, but also sub-element sized micro-cracks, as those shown in Fig. 3 b and c. These micro-cracks were detected throughout the length of the longeron after coiling, through micro-CT images.

V. Conclusions and Future Work

This paper has presented a numerically efficient finite element modeling approach for predicting damage in coilable shells made of HSC materials. The analysis was done using the ABAQUS 2020 software, and the Hashin's criterion was used for failure initiation of the different failure modes and a bilinear constitutive model was considered for damage propagation in the shell. The ply properties of interest were measured experimentally and implemented into the numerical model.

The analysis was done on a TRAC longeron shell structure made of a HSC material. The finite element predictions of damage were seen to match the experimental observations of macro and micro-cracks in the structure after coiling. Various assumptions were made at different stages of the model, which should be highlighted.

First, in the study, the tension and compression strength and fracture toughness properties of the ply were assumed to be the same. This was mainly driven by the difficulty of measuring the in situ ply strength under large curvature loads. Further studies in experimental approaches to differentiate the tension and compression strengths in the large curvature regime should be considered.

The model discussed in this study is sensitive to the strength properties of the ply. As seen in Fig. 8, small differences in the strength values (on order of 10 %), could have a large effect on the distribution of the failed elements in Fig.9 and 10. As noted earlier, because the ply strengths are in situ properties, they should be estimated carefully.

Representing the flanges of the longeron with a single shell element in the thickness direction has its limitations. Although this improves the numerical efficiency of the model, this assumption may not be the most accurate representation of the stress and strain distribution through the thickness direction. In addition, the propagation of damage through the thickness is not adequately captured under these assumptions. Instead, the damage is confined within the ply. Higher-order shell theories or using meso-scale models will increase the accuracy of the model, but at a significant cost in computational time.

Lastly, in this study, the thickness imperfection in the shell was based on assigning a laminate thickness value at an element level based on a Gaussian random number generator. However, a more accurate representation of the imperfection could be explored in the future. In addition to the thickness, other imperfections and statistical uncertainties could also be considered (volume fraction, fiber orientation, strength properties, etc.).

In conclusion, it should also be noted that a significant advantage of the simulation of coiling with damage is that it provides detailed insight into the progressive damage processes in the shell, whereas experimental observations can only be conducted after coiling, post mortem. By improving on the model in the future, this research will be useful for design and optimization studies of deployable shells for preventing material failure in HSCs.

Acknowledgments

References

[1] Block, J., Straubel, M., and Wiedemann, M., "Ultralight deployable booms for solar sails and other large gossamer structures in space," *Acta Astronautica*, Vol. 68, No. 7-8, 2011, pp. 984–992.

[2] Banik, J., Kiefer, S., LaPointe, M., and LaCorte, P., "On-orbit validation of the roll-out solar array," *2018 IEEE Aerospace Conference*, IEEE, 2018, pp. 1–9.

[3] Gdoutos, E., Leclerc, C., Royer, F., Kelzenberg, M. D., Warmann, E. C., Espinet-Gonzalez, P., Vaidya, N., Bohn, F., Abiri, B., Hashemi, M. R., et al., "A lightweight tile structure integrating photovoltaic conversion and RF power transfer for space solar power applications," *2018 AIAA Spacecraft Structures Conference*, 2018, p. 2202.

[4] Gdoutos, E., Leclerc, C., Royer, F., Türk, D. A., and Pellegrino, S., "Ultralight spacecraft structure prototype," *AIAA Scitech 2019 Forum*, 2019, p. 1749.

[5] Arya, M., Hodges, R., Sauder, J. F., Horst, S., Mobrem, M., Pedivellano, A., Wen, A., Truong, A., and Pellegrino, S., "Lightweight Composite Reflectarray that can be Flattened, Folded, and Coiled for Compact Stowage," *AIAA SCITECH 2022 Forum*, 2022, p. 1886.

[6] Soykasap, O., Karakaya, S., Gayretli, A., and Akcin, Y., "Preliminary design of deployable flexible shell reflector of an x-band satellite payload," *2nd AIAA Spacecraft Structures Conference*, 2015, p. 0945.

[7] Leclerc, C., "Mechanics of Ultra-Thin Composite Coilable Structures," Ph.D. thesis, California Institute of Technology, 2020.

[8] Cox, K., and Medina, K. A., "Scalability of triangular rollable and collapsible booms," *AIAA Scitech 2019 Forum*, 2019, p. 2026.

[9] Ferraro, S., and Pellegrino, S., "Size effects in plain-weave Astroquartz® deployable thin shells," *Journal of Composite Materials*, Vol. 55, No. 18, 2021, pp. 2417–2430.

[10] Ubamanyu, K., Ghedalia, D., Hasanyan, A. D., and Pellegrino, S., "Experimental Study of Time-dependent Failure of High Strain Composites," *AIAA Scitech 2020 Forum*, 2020, p. 0207.

[11] Lapczyk, I., and Hurtado, J. A., "Progressive damage modeling in fiber-reinforced materials," *Composites Part A: Applied Science and Manufacturing*, Vol. 38, No. 11, 2007, pp. 2333–2341.

[12] Joseph, A. P., Davidson, P., and Waas, A. M., "Open hole and filled hole progressive damage and failure analysis of composite laminates with a countersunk hole," *Composite Structures*, Vol. 203, 2018, pp. 523–538.

[13] Luo, W., and Pellegrino, S., "Propagating Instabilities in Coilable Booms," *AIAA SCITECH 2022 Forum*, 2022, p. 0407.

[14] Leclerc, C., Pedivellano, A., and Pellegrino, S., "Stress concentration and material failure during coiling of ultra-thin TRAC booms," *2018 AIAA Spacecraft Structures Conference*, 2018, p. 0690.

[15] Leclerc, C., and Pellegrino, S., "Reducing Stress Concentration in the Transition Region of Coilable Ultra-Thin-Shell Booms," *AIAA Scitech 2019 Forum*, 2019, p. 1522.

[16] Matzenmiller, A., Lubliner, J., and Taylor, R., "A constitutive model for anisotropic damage in fiber-composites," *Mechanics of materials*, Vol. 20, No. 2, 1995, pp. 125–152.

[17] Hashin, Z., and Rotem, A., "A fatigue failure criterion for fiber reinforced materials," *Journal of composite materials*, Vol. 7, No. 4, 1973, pp. 448–464.

[18] Bažant, Z. P., and Oh, B. H., "Crack band theory for fracture of concrete," *Matériaux et construction*, Vol. 16, No. 3, 1983, pp. 155–177.

[19] Jočić, E., and Marjanović, M., "Progressive failure analysis of open-hole composite laminates using FLWT-SCB prediction model," *International Journal of Mechanical Sciences*, 2022, p. 107407.

[20] Ning, X., and Pellegrino, S., "Experiments on imperfection insensitive axially loaded cylindrical shells," *International Journal of Solids and Structures*, Vol. 115, 2017, pp. 73–86.

[21] López Jiménez, F., and Pellegrino, S., "Failure of carbon fibers at a crease in a fiber-reinforced silicone sheet," *Journal of Applied Mechanics*, Vol. 80, No. 1, 2013.

[22] Arteiro, A., Furtado, C., Catalanotti, G., Linde, P., and Camanho, P., "Thin-ply polymer composite materials: A review," *Composites Part A: Applied Science and Manufacturing*, Vol. 132, 2020, p. 105777.

[23] Fernandez, J. M., and Murphey, T. W., "A simple test method for large deformation bending of thin high strain composite flexures," *2018 AIAA Spacecraft Structures Conference*, 2018, p. 0942.

[24] Sharma, A. H., Rose, T., Seamone, A., Murphey, T. W., and Lopez Jimenez, F., "Analysis of the Column Bending Test for Large Curvature Bending of High Strain Composites," *AIAA Scitech 2019 Forum*, 2019, p. 1746.

[25] Hasanyan, A. D., and Pellegrino, S., "Characterization of Interface Toughness in Thin-Ply Composites," *AIAA Scitech 2020 Forum*, 2020, p. 0694.